Analytical Model and Topology Optimization of Doubly-fed Induction Generator

Lu Sun, Haoyu Kang, Jin Wang, *Member, IEEE*, Zequan Li, Jianjun Liu, Yiming Ma, and Libing Zhou

***Abstract*—As the core component of energy conversion for large wind turbines, the output performance of doubly-fed induction generators (DFIGs) plays a decisive role in the power quality of wind turbines. To realize the fast and accurate design optimization of DFIGs, this paper proposes a novel hybrid-driven surrogate-assisted optimization method. It firstly establishes an accurate subdomain model of DFIGs to analytically predict performance indexes. Furthermore, taking the inexpensive analytical dataset produced by the subdomain model as the source domain and the expensive finite element analysis dataset as the target domain, a high-precision surrogate model is trained in a transfer learning way and used for the subsequent multi-objective optimization process. Based on this model, taking the total harmonic distortion of electromotive force, cogging torque, and iron loss as objectives, and the slot and inner/outer diameters as parameters for optimizing the topology, achieve a rapid and accurate electromagnetic design for DFIGs. Finally, experiments are carried out on a 3MW DFIG to validate the effectiveness of the proposed method.**

***Index Terms*—Doubly-fed induction generators, Accurate subdomain model, Surrogate-assisted, Transfer learning.**

I. INTRODUCTION

THE doubly-fed induction motor, known for its flexible regulation characteristics and high reliability, is widely employed in wind turbines or variable-speed pumped storage units[1]-[3]. As the proportion of wind generation capacity in the grid is steadily increasing, ensuring power quality and grid security necessitates, higher performance and stability from doubly-fed induction generators (DFIGs) [4]-[6]. However, in the system coordinated-control debugging and multi-objective optimization, it is necessary to compare the output of a large number of structural parameters, consuming a significant amount of computational time, which is not conducive to the design of motors [7]-[10]. Therefore, rapid design and optimization of DFIGs represent crucial research areas.

Currently, electromagnetic design and optimization design for DFIGs primarily rely on finite element analysis (FEA), which offers high precision but consumes significant computing time, hindering the optimization of the structural parameters. Compared to FEA, accurate subdomain model (ASM) can significantly increase computation speed, especially in multi-objective optimization, improving the efficiency of DFIG design [11]-[15]. On the other hand, ASMs, based on Maxwell equations, can account for the impact of structural parameters on electromagnetic performance and possess greater versatility compared to equivalent circuits and magnetic circuits [16]-[17]. However, to facilitate ASM modeling, it is necessary to simplify the general solution of slot vectors using boundary conditions. The slots of the stator and rotor need to be equated to sector-shaped slots parallel to the r-axis based on the principle of area equivalence. The ASM also can not consider the impact of local saturation. These assumptions will cause some errors in ASM results compared to FEA. Therefore, improvements and corrections are still needed for the ASM.

Transfer learning is an effective method to correct the errors of ASM. By using a large number of ASM calculate results as the source domain and a small number of FEA results as the target domain, training a proxy model through machine learning can effectively improve the calculation accuracy of the analytical model. At present proxy models based on transfer learning have been applied in the optimization of the topological structure of permanent magnet motors [18]-[19]. In [20]-[22], torque optimization for multi-phase permanent magnet synchronous motors is achieved through the complex conformal mapping methods and Latin hypercube methods. Furthermore, the use of transfer learning radial basis function neural network models effectively reduces the optimization difficulty of stress in high-speed motors. However, due to the lack of an analytical model for DFIGs that includes structural parameters, the dual-drive proxy model, which combines transfer learning and ASM, has not been effectively applied in the optimization.

This paper introduces a dual-driven surrogate-assisted optimization model for DFIGs, based on ASM and transfer learning. The ASM results serve as the source domain data, while the FEA results serve as the target domain data in the

Manuscript received March 18, 2024; revised April 19, 2024; accepted May 10, 2024. Date of publication June 25, 2024; Date of current version June 06, 2024.

Lu Sun, Haoyu Kang, Jin Wang, Zequan Li, and Libing Zhou are with the State Key Laboratory of Advanced Electromagnetic Technology, School of Electrical and Electronic Engineering, Huazhong University of Science and Technology, Wuhan 430074, China (e-mail: sl976763922@smail.sut.edu.cn; haoyukanghust@163.com; hustwj@126.com; hust_lzq@hust.edu.cn; zlb@mail.hust.edu.cn).

Jianjun Liu is with Dongfang Electric Machinery Co., Ltd, Dongfang Electric Corporation, Deyang, China (e-mail: liujianjun_08@126.com).

Yiming Ma is with CSG PGC Energy Storage Research Institute, Southern Power Grid Energy Storage Co., Ltd, Guangzhou 510630, China (e-mail: mayiming@ieee.org).

Lu Sun and Haoyu Kang contributed equally to this work. (*Corresponding author*: *Jin Wang*.)

Digital Object Identifier 10.30941/CESTEMS.2024.00022

transfer learning process, enhancing calculation accuracy for parallel slot structures. Based on the model, the optimization of structural parameters is carried out with the objectives of minimizing electromotive force (EMF) Total Harmonic Distortion (THD), iron loss and cogging torque. The structure of the paper is as follows: Section II establishes an ASM of the DFIGs for the magnetic flux density, EMF and loss characteristics of the generator. Section III establishes a transfer learning model to improve the optimization accuracy. Section IV calculates the electromagnetic characteristics of the generator based on the proposed model and verifies the high accuracy of the model. Section V proposes a dual-drive surrogate-assisted model for the DFIGs to carry out multi-objective optimization of the motor structural parameters. Section VI conducts experiments by manufacturing prototypes and verifies the correctness of the analytical model.

II. Establishment of ASM

A. Overview and Related Assumptions of ASM

The ASM for DFIGs is established in a two-dimensional polar coordinate system (r, θ), which is depicted in Fig. 1. The parameters of the DFIG structures can be considered in the ASM. Since the DFIGs operate only under generation conditions, the input current of the stator winding is set as 0. The following assumptions are made to establish the model:

1) The materials of the motor components are assumed to exhibit isotropic properties.

2) The stator and rotor slots are equivalent to parallel ones according to the area equivalence principle, as shown in Fig. 2.

3) The influence of saturation in both the stator and the rotor is neglected due to the considerable margin in large-scale motor design.

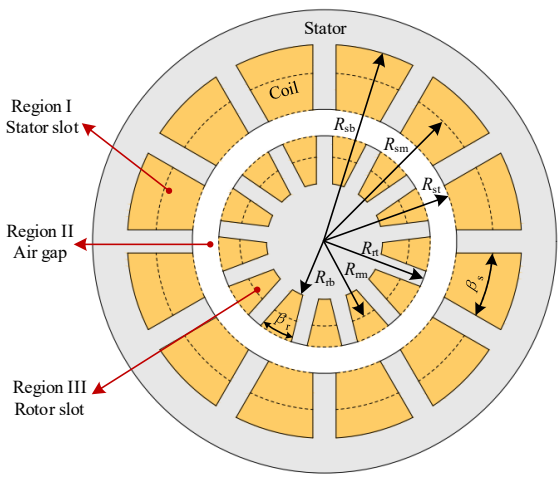

Fig. 1. ASM of DFIGs.

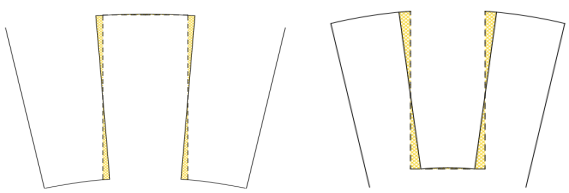

Fig. 2. Equivalent of stator and rotor slots.

B. Laplace Equation for DFIGs

The DFIGs model is divided into three regions: stator slot, air gap, and rotor slot, as illustrated in Fig. 1. The windings of the stator and rotor are adopted double-layer structures. As the permeability of the stator and rotor cores is infinite, the interface conditions can be expressed as follows.

The boundary conditions in jth/ith stator and rotor slot subdomain are:

$$\left.\frac{\partial A_{\mathrm{I}}}{\partial \theta}\right|_{\theta=\theta_{j/i}\pm\frac{\beta}{2}}=0,\quad \left.\frac{\partial A_{\mathrm{I}}}{\partial r}\right|_{R_{\mathrm{sb}}/R_{\mathrm{rb}}}=0 \tag{1}$$

Based on the Laplace equation of each subdomain, the general solution of the vector potential A in different regions is:

Bottom of region I:

$$A_{\mathrm{Ib}}=\sum_{l}A_{\mathrm{Ib}l}\left[\left(\frac{R_{\mathrm{sb}}}{R_{\mathrm{sm}}}\right)^{-\frac{l\pi}{\beta_{\mathrm{s}}}}\left(\frac{r}{R_{\mathrm{sb}}}\right)^{\frac{l\pi}{\beta_{\mathrm{s}}}}+\left(\frac{r}{R_{\mathrm{sm}}}\right)^{-\frac{l\pi}{\beta_{\mathrm{s}}}}\right]\times \cos\left[\frac{l\pi}{\beta_{\mathrm{s}}}\left(\theta+\frac{\beta_{\mathrm{s}}}{2}-\theta_{j}\right)\right]+A_{\mathrm{Ib0}} \tag{2}$$

Top of region I:

$$A_{\mathrm{It}}=\sum_{l}\left[A_{\mathrm{It}l}\left(\frac{r}{R_{\mathrm{sm}}}\right)^{\frac{l\pi}{\beta_{\mathrm{s}}}}+B_{\mathrm{It}l}\left(\frac{r}{R_{\mathrm{st}}}\right)^{-\frac{l\pi}{\beta_{\mathrm{s}}}}\right]\times \cos\left[\frac{l\pi}{\beta_{\mathrm{s}}}\left(\theta+\frac{\beta_{\mathrm{s}}}{2}-\theta_{j}\right)\right]+A_{\mathrm{It0}}+B_{\mathrm{It0}}\ln r \tag{3}$$

Region II:

$$A_{\mathrm{II}}=\sum_{n}\left[A_{\mathrm{II}n}\left(\frac{r}{R_{\mathrm{st}}}\right)^{n}+B_{\mathrm{II}n}\left(\frac{r}{R_{\mathrm{rt}}}\right)^{-n}\right]\cos(n\theta)+ \sum_{n}\left[C_{\mathrm{II}n}\left(\frac{r}{R_{\mathrm{st}}}\right)^{n}+D_{\mathrm{II}n}\left(\frac{r}{R_{\mathrm{rt}}}\right)^{-n}\right]\sin(n\theta) \tag{4}$$

Top of region III:

$$A_{\mathrm{IIIt}}=A_{\mathrm{IIIt0}}+B_{\mathrm{IIIt0}}\ln r-\frac{\mu_0 J_{\mathrm{r}} r^2}{4}+ \sum_{\nu}\left[A_{\mathrm{IIIt}\nu}\left(\frac{r}{R_{\mathrm{rt}}}\right)^{\frac{\nu\pi}{\beta_{\mathrm{r}}}}+B_{\mathrm{IIIt}\nu}\left(\frac{r}{R_{\mathrm{rm}}}\right)^{-\frac{\nu\pi}{\beta_{\mathrm{r}}}}\right]\times \cos\left[\frac{\nu\pi}{\beta_{\mathrm{r}}}\left(\theta+\frac{\beta_{\mathrm{r}}}{2}-\theta_{i}\right)\right] \tag{5}$$

Bottom of region III:

$$A_{\mathrm{IIIb}}=A_{\mathrm{IIIb0}}+\frac{\mu_0 J_{\mathrm{r}} R_{\mathrm{rb}}\ln r}{2}-\frac{\mu_0 J_{\mathrm{r}} r^2}{4}+ \sum_{\nu}\left[A_{\mathrm{IIIb}\nu}\left(\frac{r}{R_{\mathrm{rm}}}\right)^{\frac{\nu\pi}{\beta_{\mathrm{r}}}}+B_{\mathrm{IIIb}\nu}\left(\frac{r}{R_{\mathrm{rb}}}\right)^{-\frac{\nu\pi}{\beta_{\mathrm{r}}}}\right]\times \cos\left[\frac{\nu\pi}{\beta_{\mathrm{r}}}\left(\theta+\frac{\beta_{\mathrm{r}}}{2}-\theta_{i}\right)\right] \tag{6}$$

where l, n, v represent the harmonic order of the regions I, II, III respectively, A_{I0}, A_{Il}, ..., A_{IIIbv}, B_{IIIbv} are the unknown coefficients of each sub-region, and J_r is the magnetic flux density. β_s, β_r are the slot opening angles of the stator and rotor respectively.

According to the boundary conditions of the interface between each region, the undetermined coefficient A_I-B_{III} can be solved:

$$A_{\mathrm{I}t}\left(r,\theta\right)=A_{\mathrm{II}}\left(r,\theta\right),\theta_j-\frac{\beta_s}{2}\le\theta\le\theta_j+\frac{\beta_s}{2} \tag{7}$$

$$\begin{cases}H_{\mathrm{I}t\theta}\left(r,\theta\right)=H_{\mathrm{II}\theta}\left(r,\theta\right),\theta_j-\dfrac{\beta_s}{2}\le\theta\le\theta_j+\dfrac{\beta_s}{2}\\ H_{\mathrm{II}\theta}\left(r,\theta\right)=0,\text{elsewhere}\end{cases} \tag{8}$$

$$A_{\mathrm{II}}\left(r,\theta\right)=A_{\mathrm{IIIt}}\left(r,\theta\right),\theta_i-\frac{\beta_r}{2}\le\theta\le\theta_i+\frac{\beta_r}{2} \tag{9}$$

$$\begin{cases}H_{\mathrm{II}\theta}\left(r,\theta\right)=H_{\mathrm{IIIt}\theta}\left(r,\theta\right),\theta_i-\dfrac{\beta_r}{2}\le\theta\le\theta_i+\dfrac{\beta_r}{2}\\ H_{\mathrm{II}\theta}\left(r,\theta\right)=0,\text{elsewhere}\end{cases} \tag{10}$$

where H represents the magnetic field strength, and θ_j and θ_i represent the center positions of the stator and rotor slots, respectively.

All of the Fourier series coefficients can be calculated from the equations and the radial and circumferential component of the air gap magnetic field distribution depends on the coefficients A_{IIn}, B_{IIn}, C_{IIn}, D_{IIn}.

$$\begin{aligned}B_r=&-\sum_n n\left[\frac{A_{gn}}{R_g}\left(\frac{r}{R_g}\right)^{n-1}+\frac{B_{gn}}{R_r}\left(\frac{r}{R_r}\right)^{-n-1}\right]\sin(n\theta)+\\&\sum_n n\left[\frac{C_{gn}}{R_g}\left(\frac{r}{R_g}\right)^{n-1}+\frac{D_{gn}}{R_r}\left(\frac{r}{R_r}\right)^{-n-1}\right]\cos(n\theta)\end{aligned} \tag{11}$$

$$\begin{aligned}B_\theta=&-\sum_n n\left[\frac{A_{gn}}{R_g}\left(\frac{r}{R_g}\right)^{n-1}-\frac{B_{gn}}{R_r}\left(\frac{r}{R_r}\right)^{-n-1}\right]\cos(n\theta)-\\&\sum_n n\left[\frac{C_{gn}}{R_g}\left(\frac{r}{R_g}\right)^{n-1}-\frac{D_{gn}}{R_r}\left(\frac{r}{R_r}\right)^{-n-1}\right]\sin(n\theta)\end{aligned} \tag{12}$$

C. Output Characteristic of DFIGs

Based on the magnetic flux of each region, the EMF of DFIGs is:

$$E=-\frac{\mathrm{d}\int N_s B_r\mathrm{d}S}{\mathrm{d}t} \tag{13}$$

where, N_s is the number of series turns per phase of stator winding. And the THD of stator EMF is:

$$\mathrm{THD}=\frac{1}{U_f}\sqrt{\sum_{\mu_f}E_{\mu_f}^2} \tag{14}$$

where, U_f is the fundamental harmonic of stator voltage. μ_f is the order of harmonic. E_{μ_f} is the value of each harmonic voltage.

The cogging torque of the DFIGs can be deduced as:

$$T_c=\frac{L_{ef}r^2}{\mu_0}\int B_r B_\theta\mathrm{d}\theta \tag{15}$$

where, L_{ef} is the effective axial length. μ_0 is the vacuum permeability.

The efficiency of DFIGs is affected by iron loss. In DFIGs, the iron loss is divided into stator iron loss and rotor iron loss. Due to the small slip, the magnetic field speed is close to the rotor speed, and the frequency of the magnetic field cutting the rotor is very low, which makes the rotor iron loss small. Therefore, the iron loss of stator is mainly analyzed.

The iron loss can not be obtained by ASM because it is divided into tooth loss and yoke loss. In this paper, the average magnetic flux of tooth and yoke is commonly used. The magnetic flux in each component can be deduced from the vector potential of the two adjacent slots.

$$\Phi=\frac{L_{ef}}{S_{slot}}\int_{R_{st}}^{R_{sb}}\int_{\theta_j-\beta_s}^{\theta_j}A_{lj}\left(r,\theta\right)r\mathrm{d}r\mathrm{d}\theta-\frac{L_{ef}}{S_{slot}}\int_{R_{st}}^{R_{sb}}\int_{\theta_{j+1}-\beta_s}^{\theta_{j+1}}A_{lj+1}\left(r,\theta\right)r\mathrm{d}r\mathrm{d}\theta \tag{16}$$

where, S_{solt} is the area of one stator or rotor slot.

The yoke magnetic flux be obtained by the magnetic flux in a pole pitch:

$$B_y=\frac{L_{ef}R_{st}}{2L_{ef}h_{yoke}}\int_0^\tau B_{II}\mathrm{d}\theta \tag{17}$$

where, h_{yoke} is the thickness of the yoke, τ is the pole pitch angle.

Above all, in one electrical period, the average iron loss is estimated as follows:

$$P_{iron}=V_g\left[k_h B_m^2 f+\frac{\sigma L_{ef}}{12T}\int\left(\frac{\mathrm{d}B}{\mathrm{d}t}\right)^2+\frac{k_e}{T}\int\left(\frac{\mathrm{d}B}{\mathrm{d}t}\right)^{1.5}\right] \tag{18}$$

where, B_m is the amplitude of magnetic flux density, f is the frequency, T is the electrical period, σ is the conductivity, V_g is the volume of the stator or rotor iron core, k_h and k_e are the coefficient of the hysteresis loss and excess loss, respectively. The loss coefficient is tested through soft magnetic platform, measuring core loss under various magnetic flux density and frequencies, subsequently allowing for the derivation of the iron loss coefficient through fitting procedures [23].

III. Transfer Learning Model

Although the ASM significantly increases computation speed, the assumptions were made to simplify the model (in Section II A), which reduces the accuracy under some operating conditions. To improve the accuracy of the model, transfer learning is established. The results of the ASM serve as the source domain for the transfer learning model, which can correct these results. The flowchart for ASM and transfer learning is illustrated in Fig. 3.

The transfer learning Support Vector Regression (TRSVR) is used to realize the transfer learning surrogate-assisted Model using FEA Data assisted by analytical model data. The optimization object of the TRSVR is expressed as [17]:

$$\min_{w,b,\zeta,\zeta^*,\varepsilon}:\frac{1}{2}\|w_t\|^2+\frac{1}{2}\|w_s\|^2+\frac{\lambda}{2}\left[\|w_t-w_s\|^2+\left(b_t-b_s\right)\right]\times C\left[\nu\varepsilon+\frac{1}{N}\sum_{i_1}^{N_1}\left(\zeta_{i_1}+\zeta_{i_1}^*\right)+\frac{1}{N}\sum_{i_1=1+N_1}^{N}\left(\zeta_{i_1}+\zeta_{i_1}^*\right)\right]$$

$$\begin{aligned}
s.t.\ \ & w_s^T\phi\left(x_{i_1}\right)+b_s-y_{i_1}\le\varepsilon+\zeta_{i_1};i_1=1,2,...,N_1\\
& y_{i_1}-w_s^T\phi\left(x_{i_1}\right)-b_s\le\varepsilon+\zeta_{i_1}^*;i_1=1,2,...,N_1\\
& w_t^T\phi\left(x_{i_1}\right)+b_t-y_{i_1}\le\varepsilon+\zeta_i;i_1=1+N_1,2+N_1,...,N\\
& y_{i_1}-w_t^T\phi\left(x_{i_1}\right)-b_t\le\varepsilon+\zeta_i^*;i_1=1+N_1,2+N_1,...,N\\
& \zeta_{i_1},\zeta_{i_1}^*\ge 0;\varepsilon\ge 0
\end{aligned}\tag{19}$$

The coefficient R^2 is used to analyze the regression effect.

$$R^2=1-\sum_{i_1=1}^{n_1}\left(y_{i_1}-\hat{y}_{i_1}\right)^2\Big/\sum_{i_1=1}^{n_1}\left(y_{i_1}-\bar{y}_{i_1}\right)^2\tag{20}$$

The meaning of the parameters can be obtained from [17].

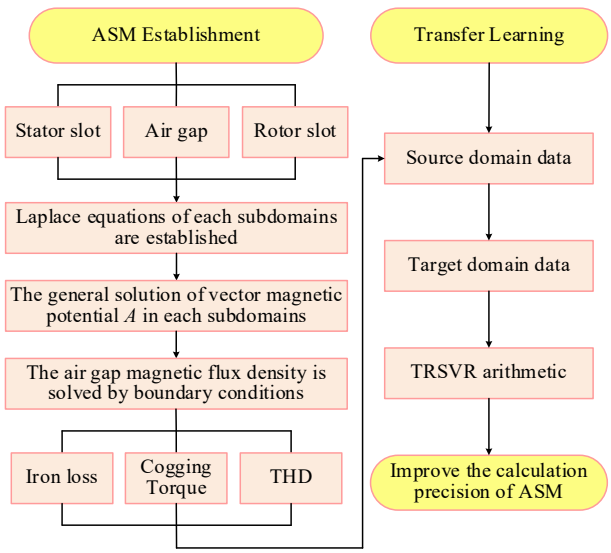

Fig. 3. The flowchart for ASM and transfer learning.

IV. Electromagnetic Characteristics of DFIG

The electromagnetic characteristic of a 3 MW DFIG is calculated by the proposed transfer learning analytical model and compared with FEA results to verify the effectiveness. The main parameters of DFIG are shown in Table I. The FEA model is shown in Fig. 4.

TABLE I
MAIN PARAMETERS OF DFIG

Parameters	Value
Rate power/MW	3
Rate frequency/Hz	50
Axial length/mm	3000
Stator slots	36
Stator outside diameter/mm	5000
Rotor outside diameter/mm	4400
Air gap length/mm	20
Rotor slots	42

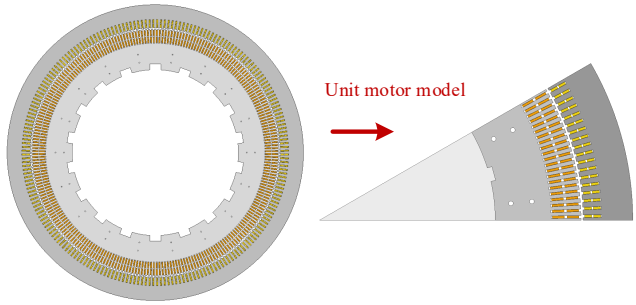

Fig. 4. FEA model of DFIG.

The magnetic flux density is analyzed under no-load operating condition in Fig. 4.

According to the comparison of magnetic flux density, the error of single ASM results is obvious due to the model simplification. From Fig. 5(a), the effective value of the magnetic flux density obtained by ASM is slightly higher than that of the FEA. According to Fig. 5(b), there are errors in the harmonic content of the magnetic flux density at frequencies of 5, 17, 19, 23, and 25.

The EMF and cogging torque of the generator are illustrated in Fig. 6 and Fig. 7.

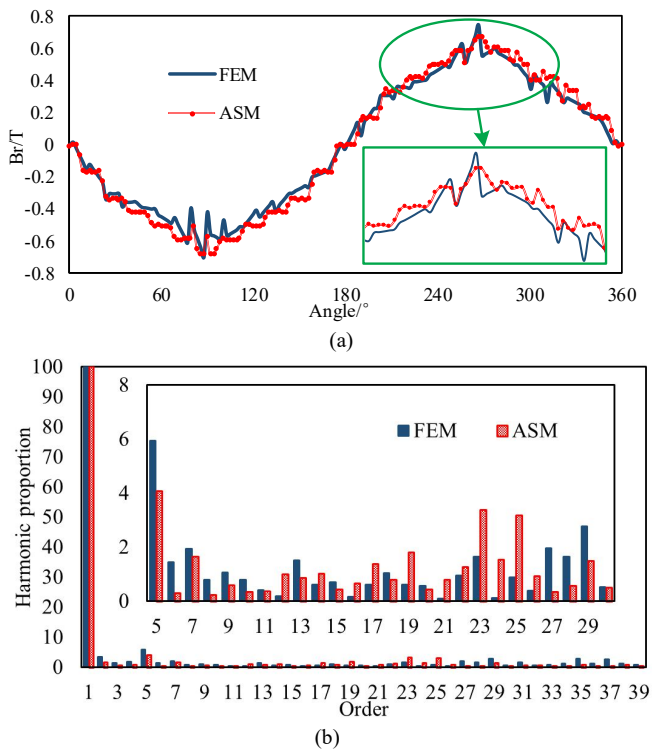

Fig. 5. Compare magnetic flux density in the air gap of DFIG. (a) Magnetic flux density. (b) Fourier decomposition of magnetic flux density.

According to the calculation results, it can be observed that the trends of the analytical model and the FEA are generally similar, but there are certain errors in both the magnitude and harmonic content. In order to achieve rapid and accurate optimization of DFIG structural parameters, a transfer learning model is adopted to improve the accuracy of the analytical model.

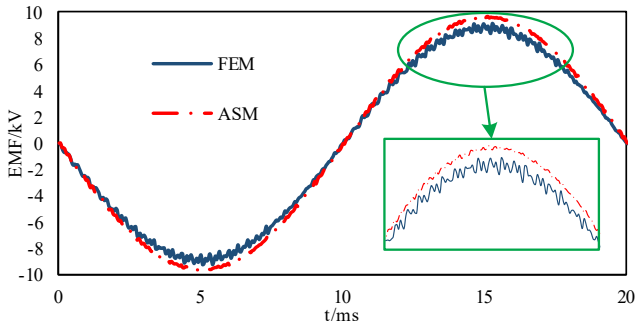

Fig. 6. Compare the EMF of DFIG.

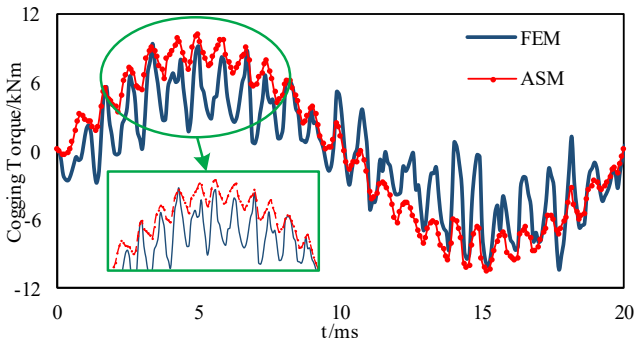

Fig. 7. Compare the cogging torque of the DFIG.

The iron loss, EMF THD, and cogging torque of DFIG are calculated and corrected using ASM and transfer learning models. The curves of the three with parameter changes are shown in Fig. 8 (taking the length of the air gap as an example).

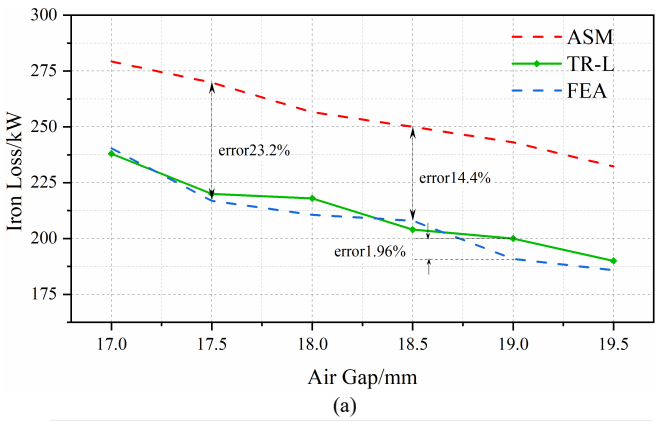

(a)

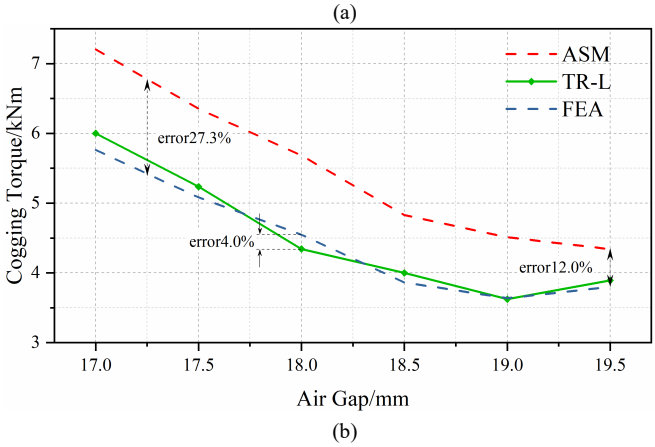

(b)

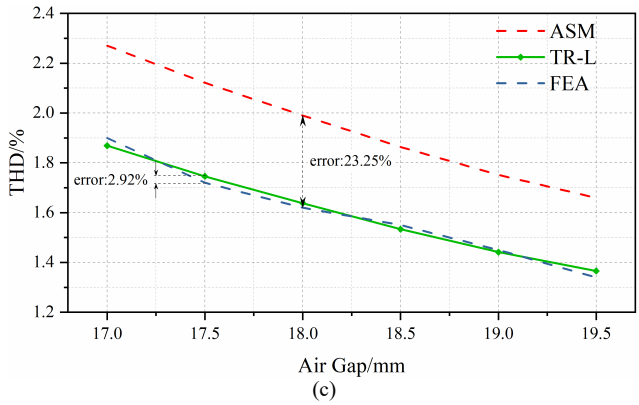

(c)

Fig. 8. Compare the electromagnetic characters of the DFIG. (a) Iron loss curve with air gap length. (b) Cogging torque curve with air gap length. (c) THD curve with air gap length.

According to the results, the errors of the electromagnetic performances are significantly reduced from about 12%-27% to 2%-4% by the transfer learning method. Especially in iron loss, due to the loss coefficient fitting, the result of ASM is with obvious errors about 40-50 kW. And the error can be reduced to about 2% after modification. Therefore, the transfer learning analytical model can improve the accuracy of the model and contribute to structural optimization.

The impact of the target domain number on the calculation accuracy of the transfer learning analytical model is further analyzed, by increasing the number of target domains from 20 to 100, and calculating the trend of the correlation coefficient R^2, as shown in Fig. 9.

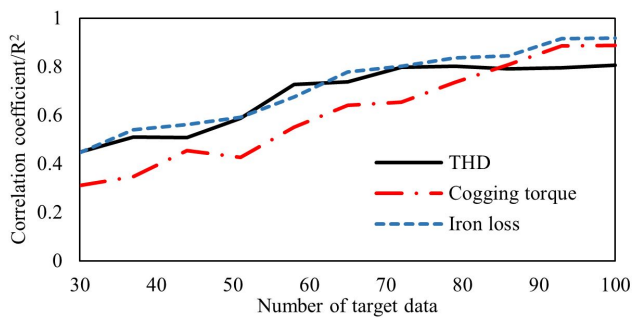

Fig. 9. Correlation coefficient comparison when target data is increased.

According to the results, in the initial stage, the accuracy of the model improved significantly as the number of target domains increased. However, when the number of target domains reached a certain level, the increment slowed down and gradually saturated. In engineering design, using too many target domains would waste computational resources. Above all, when the number of target domains exceeds 90, the precision of the three output parameters is essentially stabilized. Therefore, the target domain quantity set for this migration model is 90, effectively reducing computational costs.

V. Dual-driven Surrogate-assisted Model

Based on the above transfer model analytical model, a dual-driven surrogate-assisted model is established to optimize the structure of DFIG. NSGA-II is used as the optimization

function, and the output of the surrogate-assisted model is used as the evaluation function for the multi-objective optimization algorithm. The iron loss, EMF THD, and cogging torque are the objectives for the optimization of the structure parameters. The optimization flow chart is shown in Fig. 10.

By setting the population size to 200 and the iteration number to 1000 in the NSGA-II algorithm, the Pareto frontier is obtained, as shown in Fig. 11. The optimal design parameters are selected according to the process limitation and practical requirements.

The comparison table between the optimized parameters and the initial scheme is shown in Table II.

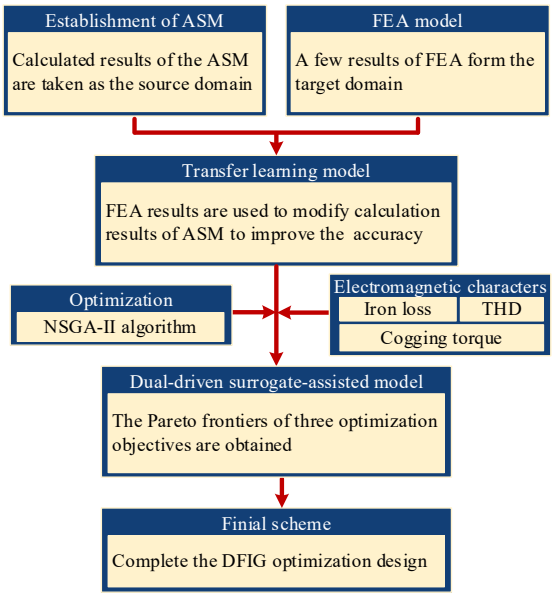

Fig. 10. Optimization model flow chart.

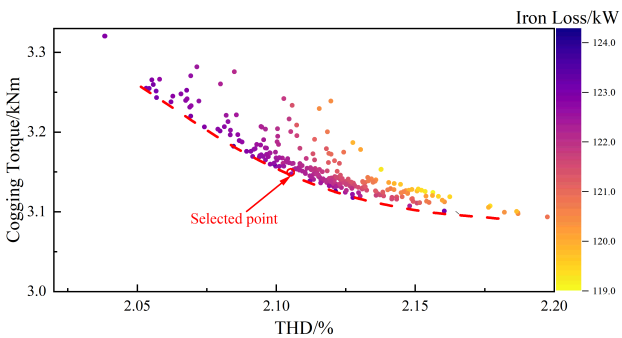

Fig. 11. Pareto frontier of the DFIG.

TABLE II
OPTIMIZATION MODEL

Parameters	Optimization	Initial
Split ratio	0.84	0.87
Stator slot height/mm	158	150
Stator slot width/mm	26.3	25.1
Rotor slot height/mm	264	257
Rotor slot width/mm	20.5	19
Air gap/mm	18	17
THD/(%)	2.1	4.26
Cogging Torque/(kN·m)	3.147	4.3
Iron loss/kW	122.6	164.8

According to the results, it can be seen that the iron loss, EMF THD, and cogging torque of the optimized DFIG are reduced by 17.9%, 21.3%, and 38.9%, respectively, which proved the effectiveness of the analytical optimization model.

VI. EXPERIMENTAL VERIFICATION

To further verify the correctness of the dual-driven surrogate-assisted optimization model based on the transfer learning analytical model, a 3 MW DFIG optimized by the model was manufactured and experimentally validated. The stator and rotor of the prototype are shown in Fig. 12. The EMF THD and cogging torque characteristics of the DFIG are tested respectively, as shown in Fig. 13.

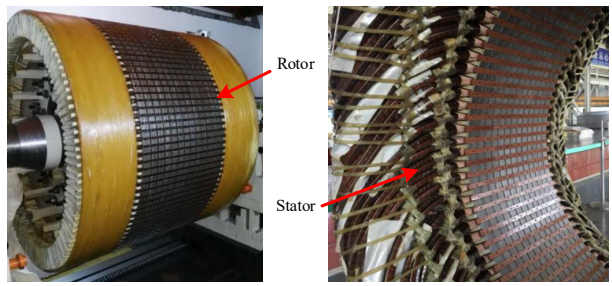

Fig. 12. The picture of the prototype rotor and stator.

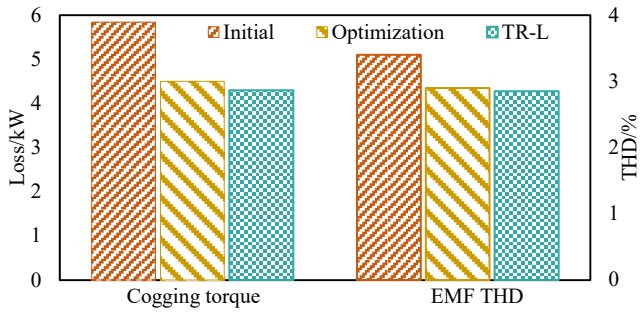

Fig. 13. The EMF THD and cogging torque characteristics.

The iron loss of the generator can not be measured directly by experimental method. Due to the slip frequency range less than 1 Hz, the magnitude difference between the rotor core iron losses and the stator core iron losses is significant, as shown in Fig. 14. Therefore, the rotor core iron losses can be neglected. Therefore, a loss separation method is used to carry out the iron loss of the DFIGs. The loss separation flow chart is shown in Fig. 15.

The mechanical loss of the DFIG is divided into air friction loss and bearing friction loss, which are calculated by using the verified analytical model. The air friction loss is:

$$P_{\text{air}} = 3.87 k_{\text{air}} \pi \eta^{1/2} \rho_{\text{air}}^{1/2} \omega^{5/2} R_{\text{st}}^{3} L_{\text{ef}} \tag{21}$$

where, k_{air} is the surface roughness coefficient of the rotor, η_{air} is the dynamic viscosity coefficient of air at one atmospheric pressure.

The bearing friction loss can be obtained as:

$$P_{\text{fb}} = 0.03 k_{\text{fb}} M_{\text{rotor}} \frac{\omega}{\pi} + 10^{-7} f_0 \left(\upsilon n_{\text{fb}}\right)^{\frac{2}{3}} d_{\text{m}}^{3} \omega \tag{22}$$

where, k_{fb} is the load factor, M_{rotor} is the mass of the rotor, f_0 is the lubrication factor, v is the working viscosity, n_{fb} is the bearing speed, and d_{m} is the average value of the inner and outer diameters of the bearing.

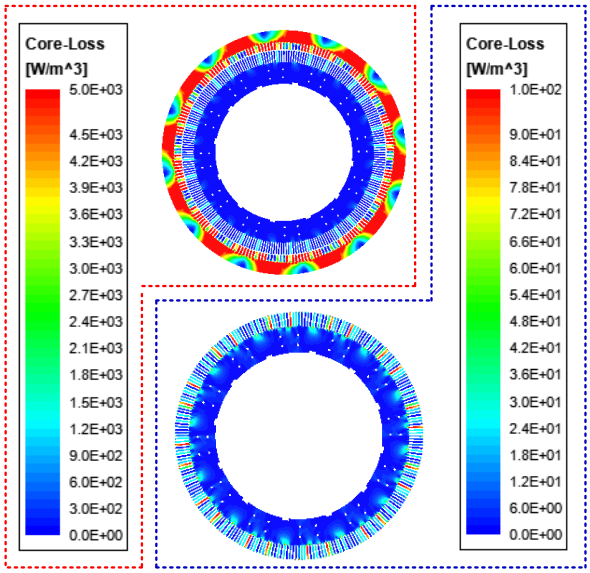

Fig. 14. The stator and rotor iron loss of the DFIG.

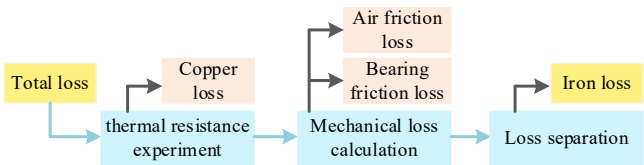

Fig. 15. Loss separation process.

The copper loss of the DFIG is obtained by measuring the thermal resistance of the windings. Due to the unavailability of thermal resistance measurements for the prototype before optimization, the winding temperature of the two motors is calculated through FEA, and the temperature of the initial DFIG is obtained proportionally. Additionally, based on the change curve of winding conductivity, the copper losses of the initial DFIG are determined.

Finally, the total loss of the motor is measured and the iron loss of the DFIG is separated. The experimental results of the iron loss are shown in Fig. 16.

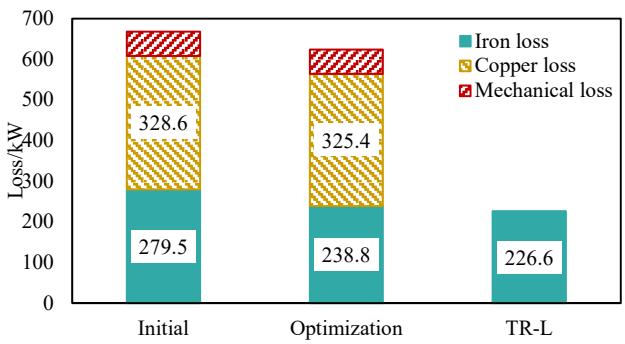

Fig. 16. Iron loss separation.

According to the results, the experimental results are in good agreement with the calculated results of the proposed analytical model. Since iron loss is difficult to measure directly, there will be some errors in the iron loss experiment and calculation, which are acceptable. The EMF THD and cogging torque results are also highly accurate. Therefore, the experimental results verify the correctness of the transfer learning analytical model and the optimization model.

VII. Conclusion

The paper proposes a highly accurate and computationally efficient multi-objective optimization method for pitch-controlled wind turbines based on ASM and transfer learning. By establishing an analytical model considering the structural parameters of the DFIGs, the computational efficiency for evaluating the performance of different electromagnetic schemes is improved. Transfer learning is employed to modify the output results of the ASM. The results indicate that transfer learning enhances the calculation accuracy. The effectiveness of the transfer learning model is validated by comparing it with FEA. Taking the stator iron loss, cogging torque, and EMF THD as targets, the structural parameters of DFIG are optimized, and a 3 MW prototype is fabricated for the experiment, thereby confirming the correctness of the optimization model.

This model is not only applicable to the electromagnetic performance analysis and optimization of DFIGs but also demonstrates versatility by enabling the replacement of the DFIGs ASM with other structural motor models. It allows rapid calculations and optimization of performance for different motor types. Thus, the model exhibits strong generality.

References

[1] B. Hu, H. Nian, and H. P. Li *et al*, "Impedance Reshaping Band Coupling and Broadband Passivity Enhancement for DFIG System," *IEEE Trans. on Power Electr.,* vol. 38, no. 8, pp. 9436–9447, Aug. 2023.

[2] S. Liang, S. Jin, and L. Shi, "Research on Control Strategy of Grid-connected Brushless Doubly-fed Wind Power System Based on Virtual Synchronous Generator Control," *CES Trans. on Electr. Mach. and Syst.*, vol. 6, no. 4, pp. 404–412, Dec. 2022.

[3] B. S. Pali, and S. Vadhera, "An Innovative Continuous Power Generation System Comprising of Wind Energy Along with Pumped-hydro Storage and Open Well," *IEEE Trans. on Sustain. Energ.*, vol. 11, no. 1, pp. 145–153, Jan. 2020.

[4] K. Ni, Y. H. Hu, and C. Gan, "Parameter Deviation Effect Study of the Power Generation Unit on a Doubly-fed Induction Machine-based Shipboard Propulsion System," *CES Trans. on Electr. Mach. and Syst.*, vol. 4, no. 4, pp. 339–348, Dec. 2020.

[5] C. M. Du, X. Du, and C. H. Tong *et al*, "Stability Analysis for DFIG-based Wind Farm Grid-connected System Under All Wind Speed Conditions," *IEEE Trans. on Ind. Appli.*, vol. 59, no. 2, pp. 2430–2445, Mar.-Apr. 2023.

[6] J. X. Ouyang, T. Tang, and J. Yao *et al*, "Active Voltage Control for DFIG-based Wind Farm Integrated Power System by Coordinating Active and Reactive Powers Under Wind Speed Variations," *IEEE Trans. on Energy Convers.*, vol. 34, no. 3, pp. 1504–1511, Sept. 2019.

[7] X. S. Tian, Y. N. Chi, and Y. Li *et al*, "Coordinated Damping Optimization Control of Sub-synchronous Oscillation for DFIG and Svg," *CSEE Journal of Power and Energy Systems*, vol. 7, no. 1, pp. 140–149, Jan. 2021.

[8] J. B. Hu, Y. H. Huang, and D. Wang *et al*, "Modeling of Grid-connected DFIG-based Wind Turbines for Dc-link Voltage Stability Analysis," *IEEE Trans on Sustain. Energy*, vol. 6, no. 4, pp. 1325–1336, Oct. 2015.

[9] X. D. Sun, N. X. Xu, and M. Yao, "Sequential Subspace Optimization Design of a Dual Three-phase Permanent Magnet Synchronous Hub Motor Based on Nsga III," *IEEE Trans. on Transport. Electrific.*, vol. 9, no. 1, pp. 622–630, Mar. 2023.

[10] G. H. Du, N. Huang, and Y. Y. Zhao *et al*, "Comprehensive Sensitivity Analysis and Multiphysics Optimization of the Rotor for a High Speed Permanent Magnet Machine," *IEEE Trans. on Energy Convers.*, vol. 36, no. 1, pp. 358–367, Mar. 2021.
[11] W. M. Tong, S. Q. Li, and X. L. Pan *et al*, "Analytical Model for Cogging Torque Calculation in Surface-mounted Permanent Magnet Motors with Rotor Eccentricity and Magnet Defects," *IEEE Tran. on Energy Conver.,* vol. 35, no. 4, pp. 2191–2200, Dec. 2020.
[12] L. J. Wu, H. Yin, and D. Wang *et al*, "A Nonlinear Subdomain and Magnetic Circuit Hybrid Model for Open-circuit Field Prediction in Surface-mounted PM Machines," *IEEE Trans. on Energy Convers.*, vol. 34, no. 3, pp. 1485–1495, Sept. 2019.
[13] Z. Q. Zhu, L. J. Wu, and Z. P. Xia, "An Accurate Subdomain Model for Magnetic Field Computation in Slotted Surface-mounted Permanent-magnet Machines," *IEEE Trans on Magn.,* vol. 46, no. 4, pp. 1100–1115, Apr. 2010.
[14] J. Ou, Y. Z. Liu, and D. W. Liang *et al*, "Investigation of Pm Eddy Current Losses in Surface-mounted PM Motors Caused by PWM," *IEEE Trans. on Power Electr.*, vol. 34, no. 11, pp. 11253–11263, Nov. 2019.
[15] P. X. Liang, F. Chai, and Y. Li *et al*, "Analytical Prediction of Magnetic Field Distribution in Spoke-type Permanent-magnet Synchronous Machines Accounting for Bridge Saturation and Magnet Shape," *IEEE Trans on Ind. Electron.*, vol. 64, no. 5, pp. 3479–3488, May. 2017.
[16] V. S. S. Kumar, and D. Thukaram, "Alternate Proof for Steady-state Equivalent Circuit of a Doubly Fed Induction Machine," *IEEE Trans. on Power Electr.*, vol. 31, no. 8, pp. 5378–5383, Aug. 2016.
[17] W. J. Chen, F. Blaabjerg, and N. Zhu *et al*, "Doubly Fed Induction Generator Wind Turbine Systems Subject to Recurring Symmetrical Grid Faults," *IEEE Trans. on Power Electron.*, vol. 31, no. 2, pp. 1143–1160, Feb. 2016.
[18] L. Shao, F. Zhu, and X. L. Li, "Transfer Learning for Visual Categorization: A Survey," *IEEE Trans. on Neural Netw. and Learn. Syst.*, vol. 26, no. 5, pp. 1019–1034, May. 2015.
[19] F. Z. Zhuang, Z. Y. Qi, and K. Y. Duan *et al*, "A Comprehensive Survey on Transfer Learning," *Proc. of the IEEE*, vol. 109, no. 1, pp. 43–76, Jan. 2021.
[20] Y. M. Ma, J. Wang, and Y. Xiao *et al*, "Transfer Learning-based Surrogate-assisted Design Optimisation of a Five-phase Magnet-shaping PMSM," *IET Electric. Power Appli.,* vol. 15, no. 10, pp. 1281–1299, Oct. 2021.
[21] B. C. Xie, Y. Zhang, and G. W. Liu *et al*, "Research on Stress Optimization of High-speed Permanent Magnet Motor Based on Fewshot Transfer Learning Surrogate Model," *Proceedings of the CSEE*, 2023. doi.org/10.13334/j.0258-8013.pcsee.230574.
[22] J. Asanuma, S. H. Doi, and H. Igarashi, "Transfer Learning Through Deep Learning: Application to Topology Optimization of Electric Motor," *IEEE Trans. on Magn.*, vol. 56, no. 3, pp. 1–4, Mar. 2020.
[23] W. M. Tong, S. Q. Li, and R. L. Sun *et al*, "Modified Core Loss Calculation for High-speed Pmsms with Amorphous Metal Stator Cores," *IEEE Trans. on Energy Convers.*, vol. 36, no. 1, pp. 560–569, Mar. 2021.

Lu Sun was born in Anshan, China, in 1995. He received the B.S. and M.S. degrees in electrical engineering from the Shenyang University of Technology, Shenyang, China, in 2018 and 2021, respectively.

He is currently studying for his PhD at Huazhong University of Science and Technology. His research interest includes modeling and optimal design of doubly-fed induction motor and modeling and suppression of rotor eddy current loss of permanent magnet machines.

Haoyu Kang was born in Yulin, China, in 2002. He obtained his bachelor's degree in electrical engineering and bachelor's degree in Economics from Huazhong University of Science and Technology in 2023.

He has been pursuing a master's degree in Department of motor and Control Engineering, Huazhong University of Science and Technology. His research focus is on the analytical modeling and optimization design of doubly-fed induction motors.

Jin Wang was born in Hebei, China in 1979. He received the B.S., M.S., and Ph.D. degrees in electrical engineering from Huazhong University of Science and Technology, Wuhan, China, in 2002, 2005, and 2010 respectively. From 2010 to 2013, he was a Postdoctoral Fellow with Huazhong University of Science and Technology.

He is currently an Associate Professor with School of Electrical and Electronic Engineering, Huazhong University of Science and Technology, Wuhan, China. His research interests include design and control of electrical machines with applications in hydroelectricity generation, pumped storage energy storage, oil and gas drilling, electric aircraft and so on.